Static and dynamic interaction between polyvinyl acetal brushes and flat surfaces : Measuring near-surface brush volume ratio and nodule volume change for moving brushes

Static and dynamic interaction between polyvinyl acetal brushes and flat surfaces—measuring near-surface brush volume ratio and nodule volume change for moving brushes

Atsuki Hosaka[1], Yuki Mizushima[1], Satomi Hamada[2], Ryota Koshino[2], Akira Fukunaga[2], and Toshiyuki Sanada[1,z,*]

[1] Department of Mechanical Engineering, Shizuoka University, Naka-ku, Shizuoka 432-8561, Japan

[2] Ebara Corporation, 4-2-1 Honfujisawa, Kanagawa 251-8502, Japan

[z] E-mail: sanada.toshiyuki@shizuoka.ac.jp

Keywords: PVA brush, Post CMP cleaning, Brush scrubbing, Wettability, Contact or noncontact cleaning.

Abstract

The cleaning mechanism for brush scrubbing, known as the contact-type cleaning method, utilizes the direct contact of impurities onto brushes or brush-induced fluid flow depending on the contact condition. Applying brush cleaning to nanosized defects in advanced semiconductor manufacturing requires understanding of the interaction between the brush and scrubbing surface under actual operating conditions. We observed the near-surface brush volume ratio and brush nodule deformation using high-speed photography to obtain insights into efficient nanosized cleaning. Evanescent fields on a prism and a convex lens facilitate the definition of the observation depths of several hundred nanometers. Starting rotation experiments revealed a drastic reduction in the brush volume ratio, indicating that the static contact is far from the dynamic contact. The volume change during roller brush nodule deformation depends on the surface material. Furthermore, large friction materials exhibit large deformation and rapid recovery. These nodule deformations may generate a different fluid flow near the surface owing to the brush's fluid absorption and desorption.

1. Introduction

Brush cleaning has been widely used for semiconductor cleaning and is indispensable, particularly for post-CMP (chemical mechanical planarization) cleaning. Polishing and slurry usage for the CMP process essentially produces impurities; thus, the PVA (polyvinyl acetal) brush is a powerful tool for cleaning flat surfaces[1-8]. The PVA brushes have very flexible

hydrophilic porous bodies, and approximately 90% of the material is porous to use a brush containing plenty of water for cleaning scrubs. Two cleaning mechanisms have been proposed for cleaning with a PVA brush, depending on the contact condition. Transferring of the impurities via direct contact or fluid share flow has been proposed as the mechanism[9-23]. Since PVA brushes are categorized as contact cleaning methods, there exists the challenge of cross-contamination from the removed impurities or from the brush itself[24-28]. In addition, a break-in treatment is required before use to prevent contamination from the brush[29-32].

The production of state-of-the-art semiconductor devices requires the removal of nanoscale impurities[33-36] to determine whether the conventional model can be applied. In particular, the scale of the brush structure was microscale; however, the cleaning target has become nanoscale in recent years. The flow is unlikely to be induced at the nanoscale because the solid surface velocity is zero. In addition, the size difference between the brush and impurities becomes large, and contact with the brush and contaminants rarely occurs.

Several AFM (atomic force microscope) studies have reported the interaction among nanoscale particles, several surfaces, chemicals, and brushes[37-38]. For example, Ikarashi et al.[38] directly measured the adhesion force of silica nanoparticles on a PVA surface in a cleaning solution. Yamada et al.[39] proposed a technique to measure the adhesion force between a PVA brush and a flat surface; however, the adhesive force that appears due to such an interaction is hardly correlated with the torque when rotating. Therefore, they speculated that the force in a static state differed from that in the sliding condition. Furthermore, Sanada et al.[40] investigated the real contact area on compressing the PVA brush to the surface and found that no contact area emerged without the skin layer case within the microscope optical resolution. Even brushes without a skin layer depicted the same order of torque as the skin layer case when rotating; thus, we speculate that the torque for the sliding condition differed from the static adhesion. Miyaki et al.[41] and Hosaka et al.[42] investigated the contact pattern of brushes and demonstrated the relationship between cross-contamination and its deformation. They concluded that the adsorption and desorption of water from the brush due to the volume change during brush deformation is crucial in surface cleaning. Therefore, we would like to know how close the brush exists to the surface to enhance the flow agitation.

Furthermore, the absolute value of the adhesive force of nanoscale particles on the

surface decreases, however reducing physical actions such as almost stagnant fluid flow caused the residues. For example, Miyaki et al.[41] reported nano-scale particles could be moved from the initial position, however, the particles could not be removed within a typical cleaning period. Ranaweera et al.[43] also shows removing nanoscale particles with a very short time of brush scrubbing, such as 10 sec. From these results, we need to clarify the flow near the wall surface which is related with the brush deformation.

In this study, we investigated how PVA brushes exist near the surface when they begin rotating from the stationary state. Applying the evanescent field and a convex lens defines the visualization depth, and the technique clarifies the brush volume ratio to that of the liquid near the surface. In addition, we estimated the brush nodule volume change during rotation related to the movement of the fluid near the wall surface. Two high-speed video cameras and collimated LED lights enabled a reconstruction of the three-dimensional nodule volume. This study shows a drastic reduction in the near-surface brush volume ratio at the start of the rotation and its relation to surface wettability.

2. Experimental Apparatus and Method

This study visualized a total internal reflection optical device to examine how the brush exists near the wall surface when it is stationary or moving. In addition, the visualization experiments of nodule shape clarify how the sliding roller brush nodule is deformed, and image analysis evaluates the volume change of the nodule. The following sections describe each experimental method. The PVA brushes used in each experiment had a skin layer. The brush was soaked in ultrapure water for at least one day before the experiment to keep the PVA brush moist. In this study, non-semiconductor materials are used for the prism and contact surface materials due to the optical restriction of visualization. The surface wettability has correlated with brush contact condition (Hara et al.)[44] and the cleaning performance (Wortman-Otto et al.)[45], so that this study uses different wettability surfaces.

2.1 Visualization of the near-surface brush volume ratio

In this study, the brushes' near-surface brush volume ratio to that of liquid (volume fraction) in the stationary or moving states under various conditions. Figure 1 shows a schematic diagram of the experimental setup that visualizes the brush volume ratio of the

PVA brushes. Different prisms—BK7 (borosilicate glass), made of glass, and PMMA (polymethyl methacrylate), made of acrylic—enabled observation of the brush volume ratio of different wettability surfaces. The contact angles of BK7 and PMMA were 28° and 61°, respectively. We set the cylindrical-type brush or roller-type brushes on the prisms, as shown in Figures 1 (a, b). Figure 1 (a) shows that the traverse actuator pushed and pulled the cylindrical brush. A motor rotated the roller-type brushes, as shown in Figure 1 (b). The optical device in Figure 1 (c) uses the principle of total internal reflection to distinguish between the solid part of the PVA brush and the liquid or gas on the prism so that the existence of the brush near the prism surface can be visualized. This method is detailed by Sanada et al.[40].

In this study, the ratio of PVA brushes near the contact surface V_{ns} was evaluated. The brush volume ratio near the surface depends on the visualization depth from the surface, that is, the binarization threshold for grayscale images (256 levels). Using a plano-convex lens installed on the prism shown in Figure 1 (c), the visualization distance was determined (refer to Shirota et al.[46] for details). Figure 2 shows the definition of the surface neighborhood brush volume ratio V_{ns} and the calculation method for the visualization distance. Figure 2 (a) shows the near-surface brush volume ratio determined as a percentage by multiplying the sum of the number of white pixels after image processing by the pixel conversion coefficient and dividing by the brush area. The plano-convex lens image in Figure 2 (b) has a grayscale, and the binarization radius r_b after binarization differs depending on the binarization threshold. The visualization distance h can be calculated from the geometrical relationship between the binarization radius and radius of curvature of the plano-convex lens. Therefore, adjusting the threshold value facilitates the determination of the visualization distance. Note that the scales in the figure for depth and surface differ by 1000 times.

We begin by observing V_{ns} when the cylindrical brush was compressed for 1, 10, 100, and 1000 s to compare the adhesion force measurements conducted by Yamada[39]. Next, we observed the temporal change in V_{ns} from the stationary to dynamic state — at the beginning of the rotation and sliding at a rotation speed of 80 rpm with both cylindrical and roller brushes. In addition, we observed the change in V_{ns} when the rotating brush contact simulated the actual brush cleaning. In all the cases, the brushes were pressed at 1 mm. As the

experimental parameters, we changed the surface wettability and visualization depth. By adjusting the incident angle φ in Figure 1 (c), the penetration depth of the evanescent wave was changed. Also, we compared the brushes under atmospheric and liquid (DI water) conditions. The images were captured at a frame rate of 60 fps and 2592 × 2048 pixels. Because the captured image was taken from an angle, the aspect ratio was corrected by image processing. Furthermore, background processing, binarization, and black/white reversals were performed to measure V_{ns} using MATLAB. Figure 3 illustrates an example of the captured image of the brush after image processing.

2.2 Volume change of nodules during rotational contact

We observed stereoscopic nodule shapes and analyzed the volume change while rotating the roller brushes. Figure 4 delineates a schematic of the experimental setup and the shape of the brush. A servomotor and L-shaped gearbox enabled the observation of the PVA roller brush as a shadow. Two high-speed video cameras and collimated LED lights were used to measure the shapes accurately. The nodule of the roller brush was vertically compressed to 1 mm at the bottom. The brush rotation speeds were set to 20 rpm and 80 rpm. Three contact materials having different wettabilities were used, namely glass, PMMA, and PTFE (polytetrafluoroethylene), with contact angles of 28°, 61°, and 97°, respectively. The images were captured at a frame rate of 300 fps and 1280 × 800 pixels.

The volume change in the nodules was estimated by reconstructing images obtained from two directions after the background subtraction, binarization, and size correction. Figure 5 shows the calculation procedure for the nodule volume. First, the bottom line of the nodule was detected, as shown in Figures 5 (a, b). Next, the nodule widths L_x and L_y in the region below the line segment were calculated for each pixel up to the contact surface. In this experiment, the nodule deformation was assumed to be small because of the small compression distance. Hence, the nodule cross-sections were assumed to maintain an ellipsoid. As shown in Figure 5 (c), an ellipse was reformed from the nodule widths L_x and L_y at each height. Finally, we reconstructed the three-dimensional nodule by stacking ellipses. The nodule volume was calculated by adding the areas of the ellipses and multiplying them by the pixel conversion factor.

The interference volume of the rigid nodule with the contact surface was used as a reference value to compare the volume changes in the nodules. Figure 6 shows a schematic of the interference volume. Let $\theta = 0°$ when the rotating rigid nodule overlapping 1 mm penetrates the contact surface. The calculation method for the interference volume differs depending on θ. When the left end of the rigid nodule does not penetrate the contact surface, as shown in Figure 6 (b), the interference volume can be calculated by calculating the volume of the hoof-shaped cylinder. In addition, when the left side of the rigid nodule penetrates the contact surface, as shown in Figure 6 (c), the interference volume can be calculated by calculating the volume when the cylinder is cut diagonally. We also compared the nodule entrainment angle α, as shown in Figure 6 (a).

3. Results

3.1 Visualization of the near-surface brush volume ratio

Figure 7 shows that the relative increase in V_{ns} for $t = 1$ s when pressed the cylindrical brush for a long time. From Figure 7 (a), it is evident that V_{ns} is increased slightly over time in the atmosphere. The increase rate of V_{ns} is larger on the BK7 prism than on the PMMA prism. Furthermore, from Figure 7 (b), V_{ns} hardly changed in water. In the experiment of adhesive force measurement by Yamada et al.[39], the adhesion force increased over time, and the adhesion force was twice as different between 1 s and 1000 s. The overall V_{ns} is almost unchanged, which is contrary to the expectation. Notably, the brush area increased and decreased in some places in observing the captured image, and the brush structure was gradually moving even in the stationary state.

Figure 8 shows the results of observing the brush near the surface when it started rotating at 80 rpm from a stationary state. It is evident that the rotating V_{ns} is significantly lower than the stationary V_{ns}, as shown in Figure 8 (a). When the rotation started at $t = 0$ s, the white part decreased from the outside, where the speed was fast, as shown in Figure 8 (b). These facts indicate that the brush near the surface moves away from the surface during rotation.

Table 1 and Figure 9 show the V_{ns} with different visualization distances for liquid and atmospheric cases, same as Fig. 8, i.e. when it started rotating from a stationary state. Rotating V_{ns} is again significantly lower than the stationary V_{ns}. Besides, both rotating and

stationary V_{ns} decreased with the decrease of visualization depth.

Next, we compare the V_{ns} reduction between the stationary and sliding conditions, as shown in Figs 8 and 9, for cylindrical and roller brushes under various conditions. Table 2 and Figure 10 show the comparison conditions and the results for V_{ns} change when the brushes are moving. V_{ns} at the stationary condition on the PMMA prism is larger than that on the BK7 prism based on the results of the same visualization distance of 300 nm in liquid (case a to d). V_{ns} on the rotating cylindrical brush on PMMA (case b) is larger than those on the BK7 prism (case a). In contrast, V_{ns} on the sliding of the roller brushes is almost identical for both prisms (cases c and d). Thus, V_{ns} is material-dependent. In addition, V_{ns} exhibited a large difference between cylindrical and roller brushes under stationary conditions. The atmospheric condition increases V_{ns} under both stational and rotating conditions, although the visualization distance is smaller than in the liquid case (cases a and e). In addition, V_{ns} increased as the visualization distance increased (cases a, f, and g).

Subsequently, we measured the V_{ns} change in contact with a cylindrical brush under rotation, which simulates the actual cleaning process. Figures 11 (a, b) depict the results of contacting the brush with the prism while rotating, and V_{ns} at the time of rotational contact show similar trends as in Figure 10. V_{ns} was smaller than that of the stationary condition and was larger on the PMMA prism. We then emphasize the V_{ns} change when the rotating brush is stopped. Hence, V_{ns}, particularly BK7, increased, as clearly confirmed at position (ii) in Figures 11 (b, c). However, V_{ns} is far from the stational condition. In addition, we confirmed that the brush gradually rotated when the brush was stopped and lifted, indicating that the twisted brushes were rotating. We attached the video in the supplementary material[45] because confirming this phenomenon with images was challenging.

3.2 Volume change in nodules during the rotational contact

Figure 12 shows an example of the reconstruction of the nodules by stereo imaging of the sliding roller-type brush. It is evident that the reconstruction of the nodules by ellipse approximation is successful. Figure 13 shows the law images when a roll-type brush is slid over three different wettability materials. From (i) to (iv) in Figure 13 (a), the front side of the nodule was pulled into the contact surface when the edge of the nodule came in contact.

Thereafter, the nodule slides the contact surface in (v) – (vii) while maintaining entrainment. Then, the nodule side was released from the contact surface and recovered rapidly between (viii) and (ix). Finally, the nodule shape returned to its original shape when separated from the surface (x). Figure 13 (b) zooms in on Figure 13 (a). Here, we define the nodule front angle to surface α between the front side face of the nodule and the contact surface. The angles shown from (iii) to (v) in Figure 13 (b) were almost constant, and the brush moved while maintaining the entrainment side face during sliding. Figure 13 (c) shows the temporal change in the angles for the different contacting materials. The initial angle at contact (t = 0 s) was almost the same as that of the rigid nodule. However, the angle gradually decreased over time and quickly increased, approaching the rigid nodule (t ~ 0.5 s).

Figures 14 (a, b) show the nodule volume changes at different speed rotations. Overall, the experimentally obtained volume change shows a large volume change compared to the interference volume of a rigid nodule. The volume gradually decreased at the beginning of compression, reached a maximum, and recovered rapidly. Sliding on PMMA showed the largest volume change. Glass and PTFE have different wettabilities; however, a similar volume change is observed. The material dependence is more clearly observed in the low-rotation cases.

4. Discussion

We begin by discussing why V_{ns} hardly changed when the cylindrical brush was compressed for a long time. Yamada et al.[39] showed that (1) the adhesive force increased as the brush contact time increased and (2) increasing the nanoscale contact point caused an increase in the adhesive force. The brushes observed in this study are brushes located at a depth of several hundred nanometers from the surface and are merely on an optically observable scale. Therefore, we considered that the adhesive force measured by Yamada et al. is due to the interaction between the polymer chain existing on the surface of the PVA brush and the surface, which is a force on a micro-scale that is hardly observed in this study.
We then discuss that V_{ns} at the brush movement was significantly lower than that during stationary. In this study, we observed the existence of the brush near the surface from 100 nm to 525 nm and found almost no brush near the surface when the brush was rotating and

sliding. This study observed using with skin-layer brushes. The long-term use of the brush can sometimes remove the skin layer on the brush surface. Since the skin layer is a high-density layer with a lower porosity than the internal structure of the brush, it becomes closer to non-contact when removing the skin layer. We have also observed the without skin-layer brushes and found almost zero brush existence ratio near the surface. Even significant lower V_{ns} observed with rotating skin layer brushes, we believe that both long-term used and without skin layer brushes mainly conducted non-contact cleaning. These results indicate that the conventional cleaning model, wherein particles directly adhere to the solid part of the brush are removed, is hardly applied to nanoscale contaminants. We believe that the fluid motion induced by the brush is more essential for small contaminants. Increasing the visualization distance increased V_{ns}. Therefore, the conventional cleaning model, that is, the direct particle removal by brush attachment, is sufficient to apply several micrometer-scale contaminants.

Subsequently, the effect of wettability on the V_{ns} difference is discussed. We consider that the water existing on the poor wettability prism, such as PMMA, easily moves to the brush side. This is because the PVA brush is hydrophilic and can absorb substantial water. Therefore, the brushes easily approached the prism surface and showed strong interactions with each other. Therefore, a larger V_{ns} on PMMA emerged compared to V_{ns} on BK7. The torques rotating on brushes measurements by Yamada et al[39] showed the same tendency where a larger torque on PMMA emerged compared to that of BK7. The results of Hara et al.[44] and Ito et al.[49] also support this consideration.

Furthermore, we considered the effect of liquid media on V_{ns}. In general, the van der Waals interactions between the material and substrate significantly decrease in aqueous media. V_{ns} under atmospheric conditions yielded a large value in both stationary and rotating conditions compared to the submerged in liquid case. We consider that water is always present between the brush and prism surface under submerged conditions, and the water weakens this interaction. Therefore, the brush and the surface easily interact with each other in the absence of water, so that there are many brushes near the surface, and thus V_{ns} becomes a large value.

We consider that the V_{ns} contacting the cylindrical brush were rotated, stopped, and

pulled up. Figures 10 and 11 show the same V_{ns} tendency between the brush contacting with rotation and rotation starting from a stationary state. These results indicate that there is almost no brush near the surface during rotation, regardless of the contact method. Next, we discuss increasing V_{ns}, which was particularly observed on BK7 when the rotating brush was stopped. For this phenomenon, we anticipated that hydrogen bonds are involved. The BK7 prism is a type of glass; thus, it has a larger hydrogen bond than PMMA. We consider that the polar surface groups interact more strongly at low-speed rotation or stationary state than at high-speed rotation. The hydrogen bond, which is one of the interactions with the surface, is strengthened[3]. Therefore, V_{ns} increased more on BK7, which has a strong hydrogen bond when the brush stops rotating. After lifting the brush, the brush was gradually rotated, which indicates that the twisting brush rotated. In the present visualization method, nanoscale interactions, such as hydrogen bond[3], polymer adsorption, and roop-train-tail structure[50-51], were impossibly measured due to the camera's resolution. Although the small V_{ns} is observed during rotation, the twisted brush shows that the surface and brush interact during rotation. We consider this to be similar to gel friction[52-54].

Finally, we discuss the volume changes in the brush nodules. Because no brush existed near the contacting surface, we consider that the movement of the liquid near the surface is also crucial for cleaning. First, the experimentally obtained volume change confirmed a large volume change compared to the interference volume of the rigid nodule. During the contact, the front of the nodule was pulled into the cleaning surface so that the nodule was more deformed, resulting in a volume change different from the interference volume. Second, the volume gradually decreased at the beginning of the contact, the decline in the volume reached a maximum, and the volume recovered rapidly. Thus, the volume change was asymmetrical, in contrast to the interference volume. In the case of symmetrical deformation, the water inside the brush is desorbed to the outside during the contact, and the water is absorbed inside the brush at the time of recovery for its original shape. We believe that it may be effective for cleaning in the case of asymmetric deformation because it changes the water absorption and desorption.

Xu et al.[15] showed that the cleaning efficiency differed between the forward and reverse rotations of the brush against the wafer rotation. We have obtained similar results in

nanoparticle cleaning tests. We consider that this is due to the brush deformation. The volume decreases rapidly and slowly recovers during the brush contacting. Accordingly, the water contained brushes desorbed rapidly. After that, the brush absorbed water containing nanoparticles near the surface. Therefore, large relative velocity rotation enhances the cleaning and vice versa.

Third, let us consider the dependence of the contact surface material on the volume change. In the experiment, the maximum volume change was observed when sliding on PMMA. When the nodule slides, the brush is deformed and dragged. PMMA has a long interaction with the brush, the nodule is pulled into the contact surface, and the volume is significantly reduced. Wortman-Otto et al. [45] reported that surface energy is highly correlated with cleaning efficiency. We believe that the relationship between surface energy and cleaning efficiency is caused by water absorption and desorption from the nodule. The frictional force due to wettability shown by Hara et al.[44] and the difference in the volume change of nodule deformation shown in this study is crucial to nanosized contaminant cleaning.

5. Conclusion

The brush scrubbing technique, which is a promising candidate for post-CMP cleaning of state-of-the-art semiconductor device manufacturing, requires removing nanoscale impurities. However, the size difference between the brush and impurities is significant, and contact between the brush and contaminants hardly occurs. Therefore, we examined how close the brush exists to the surface. In this study, we established a visualization method to investigate the brush volume ratio near the surface. In addition, we estimated the volume change in the brush nodules during rotation related to fluid movement near the wall surface due to absorption and desorption from the brush.

The visualization method used the evanescent field and convex lens, facilitating the calculation of the near-surface brush volume ratio. In addition, high-speed stereo photography of the rotating brush nodule was used to reconstruct a three-dimensional nodule shape to obtain the volume change. Thus, the experiments revealed a reduction in the near-surface brush volume ratio when moving and even when it interacted with the surface. The brush was

twisted during rotation, and the near-surface brush volume ratio was related to surface wettability. The side face of the rotating brush nodules was pulled into the contact surface, and the volume was significantly reduced. Then, the brush quickly returned to its original shape. These results indicate that a very limited brush exists near the surface when moving, providing insights into the non-contact cleaning of the brush scrubbing for nanometer-scale particles. In addition, the fluid near the wall surface possibly moved due to the change in the volume of the brush nodules during rotation.

The results imply that non-contact removal is essential for nanoscale particles, although direct contact removal is dominant for micro-scale particles. Therefore, surface wettability and the presence or absence of a liquid film are critical because they cause the brushes to approach the cleaning surface during brush scrub cleaning. In this study, we investigated the visualization and volume changes of brushes on non-semiconductor materials. In the future, we plan to investigate the near-surface brush volume ratio and the state of volume change observed during actual semiconductor cleaning.

Acknowledgments

The authors thank Dr. Hirokuni Hiyama and Dr. Chikako Takatoh of Ebara Corporation for their fruitful discussions.

References

1. G. M. Burdick, N. S. Berman, and S. P. Beaudoin, *J. Electrochem. Soc.*, **150** (10), G658-G665 (2003).

2. Y. Ein Eli and D. Starosvetsky, *Electrochim. Acta*, **52** (5), P1825-P1838 (2007).

3. D. Ng, and H. Liang, *J. Tribol.*, **130** (2), 021603 (2008).

4. A. Philipossian and T. Sun, *Electrochem. Solid-State Lett.*, **12** (3), H84-H87 (2009).

5. T. Sun, Y. Zhuang, W. Li and A. Philipossian, *Microelectron. Eng.*, **100**, P20-P24 (2012).

6. M. Keswani, and Z. Han, Developments in Surface Contamination and Cleaning, 8, R. Kohli and K.L. Mittal, Editor, P. 156-163, Elsevier, Amsterdam (2015).

7. S. Sahir, N. P. Yerriboina, S. Y. Han, K. M. Han, T. G. Kim, N. M., J. G. Park, *Appl. Surf. Sci.*, **545**, 149035 (2021).

8. C. F. Graverson, K. M. Wortman-Otto, A. N. Linhart, Y. Sampurno, A. Philipossian, J. J.

Keleher, *Mater. Chem. Phys.,* **259**, 124170 (2021).

9. G. Zhang, G. Burdick, F. Dai, T. Bibby and S. Beaudoin, *Thin Solid Films*, **332** (1-2), P379-P384 (1998).

10. F. Zhang and A. Busnaina, *Appl. Phys. A: Mater. Sci. Process.*, **69** (4), P437-P440 (1999).

11. F. Zhang, A. A. Busnaina and G. Ahmadi, *J. Electrochem. Soc.*, **146** (7), P2665-P2669 (1999).

12. G. M. Burdick, N. S. Berman and S. P. Beaudoin, *J. Nanopart. Res.*, **3** (5), P453-P465 (2001).

13. A. A. Busnaina, H. Lin, N. Moumen, J. W. Feng and J. Taylor, *IEEE Trans. Semicond. Manuf.*, **15** (4), P374-P382 (2002).

14. G. M. Burdick, N. S. Berman and S. P. Beaudoin, *J. Electrochem. Soc.*, **150** (2), G140-G147 (2003).

15. K. Xu, R. Vos, G. Vereecke, G. Doumen, W. Fyen, P. W. Mertens, M. M. Heyns, C. Vinckier and J. Fransaer, *J. Vac. Sci. Technol. B*, **22** (6), P2844-P2852 (2004).

16. K. Xu, R. Vos, G. Vereecke, G. Doumen, W. Fyen, P. W. Mertens, M. M. Heyns C. Vinckier, J. Fransaer and F. Kovacs. *J. Vac. Sci. Technol. B*, **23** (5), P2160-P2175 (2005).

17. G. M. Burdick, N. S. Berman and S. P. Beaudoin., *The solid Films*, **488** (1), P116-P123 (2005).

18. D. Ng, P. Y. Huang, Y. R. Jeng and H. Liang, *Electrochem. Solid-State Lett.*, **10** (8), H227-H231 (2007).

19. Y. Huang, D. Guo, X. Lu and J. Luo, *Appl. Surf. Sci.*, **257** (7), P3055-P3062 (2011).

20. Y. Huang, D. Guo, X. Lu and J. Luo, *Wear*, **273** (1), P105-P110 (2011).

21. X. Gu, T. Nemoto, Y. Tomita, A. Teramoto, S. Sugawa and T. Ohmi, *Jpn. J. Appl. Phys.*, **50** (5S1), 05EC07 (2011).

22. X. Gu, T. Nemoto, Y. Tomita, A. Teramoto, S. Sugawa and T. Ohmi, *J. Electrochem. Soc.*, **158** (11), H1145-H1151 (2011).

23. Y. T. Huang, Y. Li, D. Guo and C. L. Meng., *Sci. China: Tech. Sci.*, **56** (12), 2994-3000 (2013).

24. N. Sato and Y. Shimogaki, *J. Electrochem. Soc.*, **158** (11), D651-D656 (2011).

25. H. J. Kim, G. Bohra, H. Yang, S. G. Ahn, L. Qin and D. Koli, *Microelectron. Eng.*, **136**,

P36-P41 (2015).

26. H. J. Kim, B. Egan, X. Shi, J. H. Han, *ECS J. Solid State Sci. Technol.*, **7** (11), P693-P697 (2018).

27. J. H. Lee, M. Purushothaman, K. M. Han, H. Y. Ryu, N. P. Yerriboina, T. G. Kim, Y. Wada, S. Hamada, H. Hiyama, J. G. Parka, *Polymer Testing*, **77**, 105921 (2019).

28. J. H. Lee, M. K. Poddar, K. M. Han, H. Y. Ryu, N. P. Yerriboina, T. G. Kim, Y. Wada, S. Hamada, H. Hiyama, J. G. Park, *Polymer Testing*, **90**, 106669 (2020).

29. J. H. Lee, H. Y. Ryu, J. K. Hwang, N. P. Yerriboina, T. G. Kim, S. Hamada, Y. Wada, H. Hiyama, J. G. Park, *ECS J. Solid State Sci. Technol.,* **8** (6), P307-P312 (2019).

30. J. H. Lee, M. K. Poddar, N. P. Yerriboina, H. Y. Ryu, K. M. Han, T. G. Kim, S. Hamada, Y. Wada, H. Hiyama, J. G. Park, *Polymer Testing*, **78**, 105962 (2019).

31. J. H. Lee, H. Y. Ryu, J. K. Hwang, N. P. Yerriboina, T. G. Kim, S. Hamada, Y. Wada, H. Hiyama, J. G. Park., *ECS J. Solid State Sci. Technol.*, **8** (6), P307 (2019).

32. B. Withers, C. Hughes, Y. Luo, H. Chen, E. Nelson, B. Best, J. H. Jeon., *ECS J. Solid State Sci. Technol.,* **8** (12), P794 (2019).

33. S. Hong, J. Kim, J. Won, N. Qureshi, S. Chae, Y. Wada, H. Hiyama, S. Hamada, T. Kim., *ECS J. Solid State Sci. Technol.*, **8** (8), P430 (2019).

34. I. C. Choi, H. T. Kim, N. P. Yerriboina, J. H. Lee, L. T., T. G. Kim, J. G. Park, *ECS J. Solid State Sci. Technol.*, **8** (5), P3028-P3034 (2019).

35. N. Handa, H. Hiyama, K. Amagai and A. Yano., *ECS J. Solid State Sci. Technol.,* **9** (6), 064001 (2020).

36. C. Li, D. Zhao, L. Xie, X. Lu., *ECS J. Solid State Sci. Technol.*, **9** (2), 023002 (2020).

37. J. G. Park, S. H. Lee, J. S. Ryu, Y. K. Hong, T. G. Kim, A. A. Busnaina, *J. Electrochem. Soc.*, **153** (9), G811-G814 (2006).

38. T. Ikarashi, T. Yoshino, N. Nakajima, K. Miyata, K. Miyazawa, Y. M. Jaques, A. S. Foster, M. Uno, C. Takatoh, T. Fukuma, *ACS Appl. Nano Mater.,* **4** (1), P71-P83 (2020).

39. K. Yamada, Y. Mizushima, S. Hamada, A. Fukunaga, H. Hiyama, T. Sanada., *ECS J. Solid State Sci. Technol.*, **8** (11), P740 (2019).

40. T. Sanada, M. Hanai, A. Fukunaga, H. Hiyama, *Solid State Phenom.*, **282**, P73-P76 (2018).

41. T. Miyaki, Y. Mizushima, S. Hamada, R. Koshino, A. Fukunaga, T. Sanada., *Solid State Phenom.*, **Vol. 314**. P253-258 (2021).

42. A. Hosaka, T. Miyaki, Y. Mizushima, S. Hamada, R. Koshino, A. Fukunaga, T. Sanada., *J. Photopolym. Sci. Technol.*, **Vol. 34**. 505-509 (2021).

43. C. K. Ranaweera, P. Khajornrungruang, S. Hamada, A. Gowda, H. Vegi, J. Seo1, and S. V. Babu, *ECS J. Solid State Sci. Technol.*, **10** (8), 084004 (2021).

44. Y. Hara, T. Sanada, A. Fukunaga and H. Hiyama, *ECS J. Solid State Sci. Technol.*, **4** (5), P141-P148 (2015).

45. K. M. Wortman-Otto, A. N. Linhart, A. M. Mikos, K. A. Cahue, J. J. Keleher, *Solid State Phenom.*, **314**, P237-P246 (2021).

46. M. Shirota, M. A. J. van Limbeek, D. Lohse, C. Sun, *Eur. Phys. J. E*, **40** (5), P54 (2017).

47. See supplementary material for movie corresponding to Fig. 8 (b), recording rate: 60fps, 1/6 times playback speed.

48. See supplementary material for movie corresponding to Fig. 10 (c), recording rate: 60fps, normal playback speed.

49. M. Ito, T. Sanada, A. Fukunaga and H. Hiyama, *ECS J. Solid State Sci. Technol.*, **7** (4), P201-P208 (2018).

50. T. Isobe, M. Nakanome, K. Nakazono, S. Matsushita, A. Nakajima, *Ceramics International,* **39** (4), P3857-P3864 (2013).

51. D. Corinna, B. T. Stokke, R. S. Dias, *Polymers,* **11** (2), P275 (2019).

52. J. Gong, M. Higa, Y. Iwasaki, Y. Katsuyama, Y. Osada., *J. Phys. Chem. B*, **101** (28), P5487-P5489 (1997).

53. G. Jianping, Y. Osada., *J. Chem. Phys.*, **109** (18), P8062-P8068 (1998).

54. N. Sato, Y. Aoyama, J. Yamanaka, A. Toyotama, T. Okuzono, *Scientific reports,* **7** (1), 6099 (2017).

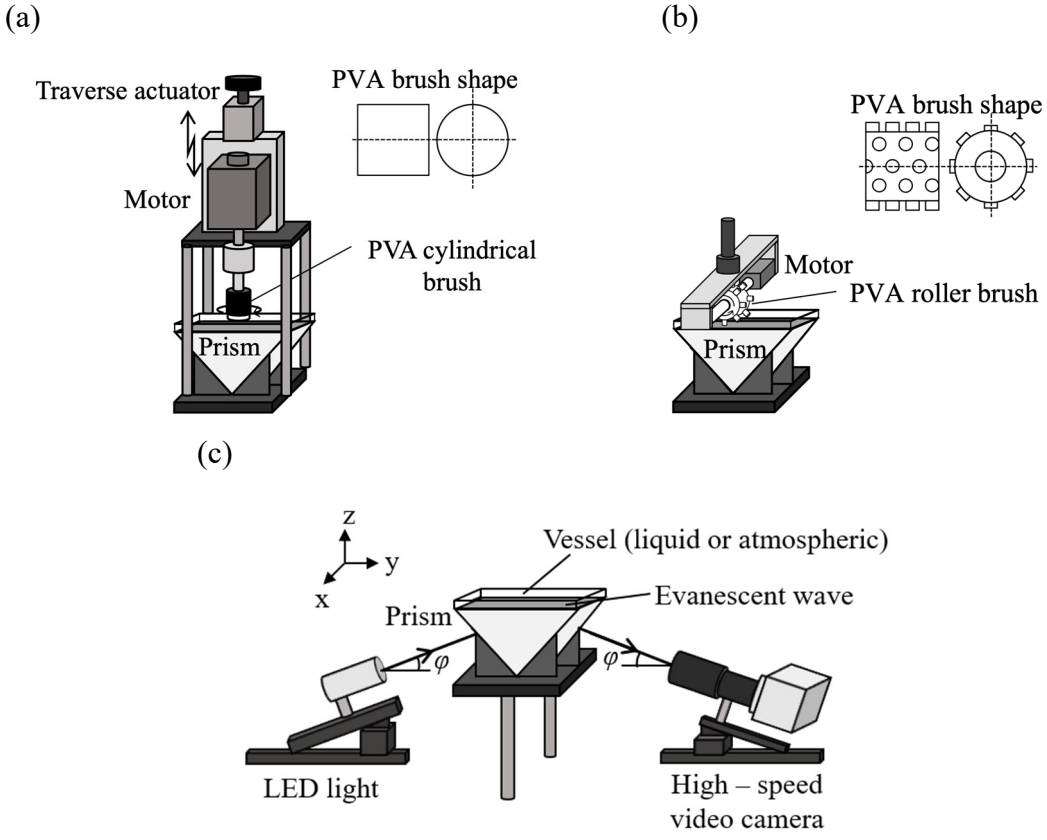

Figure 1. Schematic diagram of the experimental setup: (a) Cylindrical brush drive unit, (b) Roller brush drive unit, (c) Total internal reflection optical device.

.

(a)

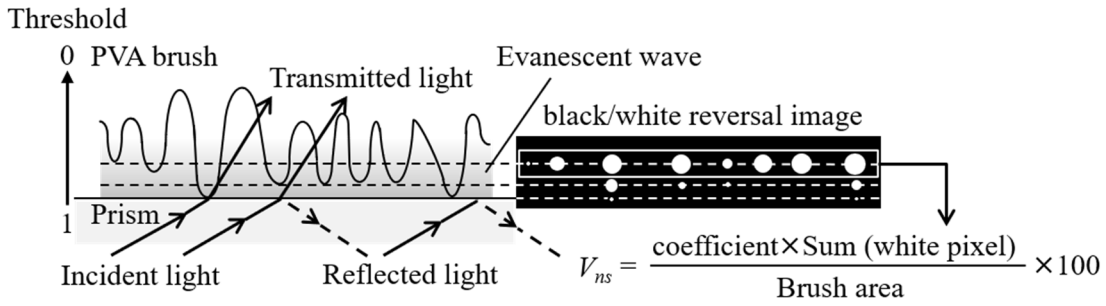

(b)

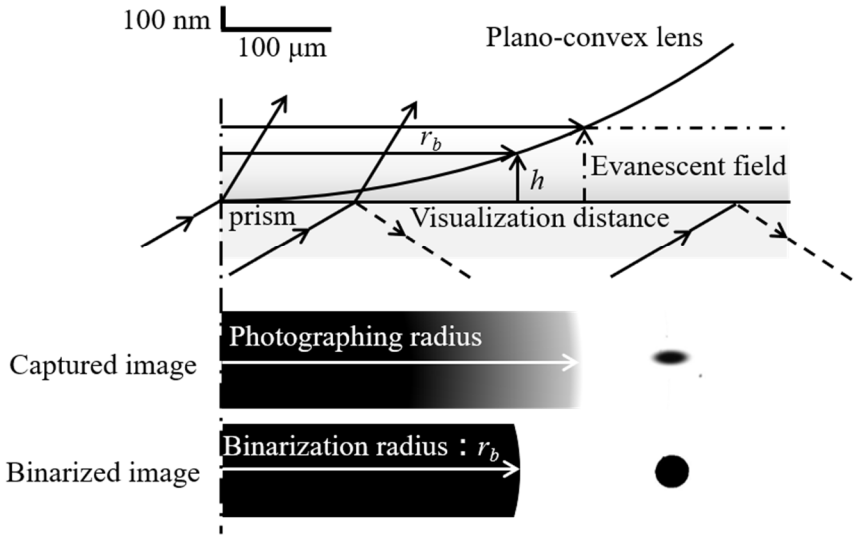

Figure 2. Principle of imaging with evanescent waves: (a) Definition of the near-surface brush volume ratio V_{ns}, (b) Calculation method of the visualization distance.

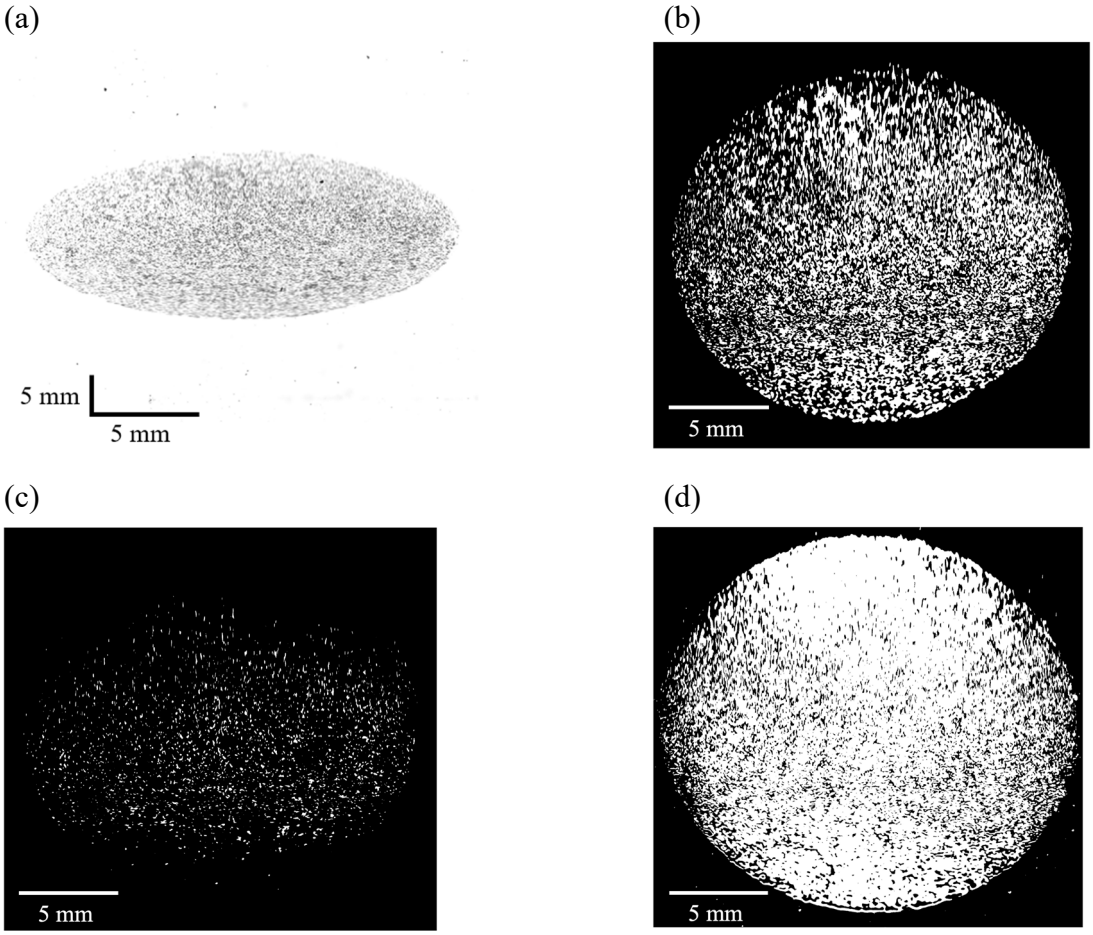

Figure 3. Typical images of the cylindrical brush on BK7 prism: (a) captured image in liquid condition, (b)-(d) aspect ratio correction, background processing, binarization, and black/white reversal. Conditions were (b) visualization distance h = 300 nm in liquid, (c) h = 100 nm in liquid, and (d) h = 100 nm in atmospheric condition.

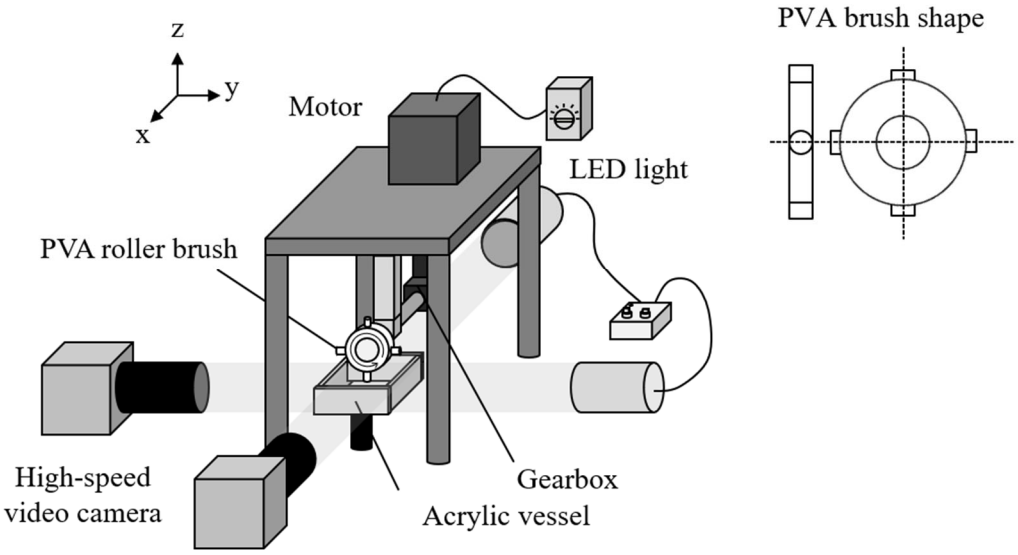

Figure 4. Schematic of the nodule deformation observation setup.

(a) and (b)

(c)

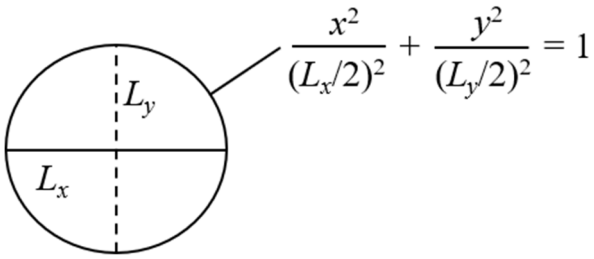

Figure 5. Calculation method of the nodule volume, image after processing (a) in the *x*-direction, (b) in the *y*-direction, (c) reconstruction of the nodule by staking the ellipses.

(a)

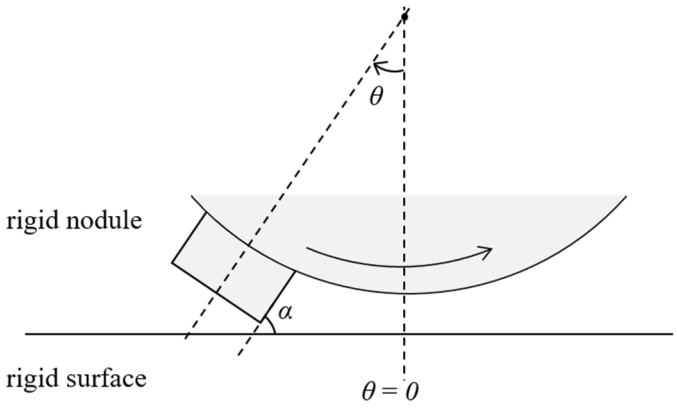

(b)

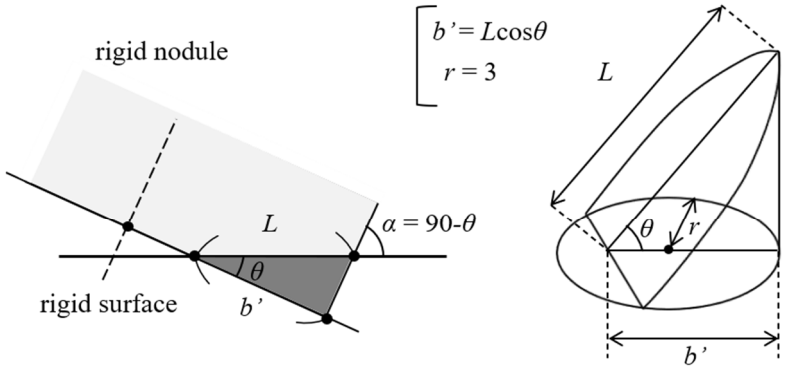

$$V = \tan\theta/3 \cdot [\sqrt{r^2-(r-b')^2} \cdot \{2r^2+(r-b')^2\}+3r^2(b'-r)\cdot\cos^{-1}(r-b'/r)]$$

(c)

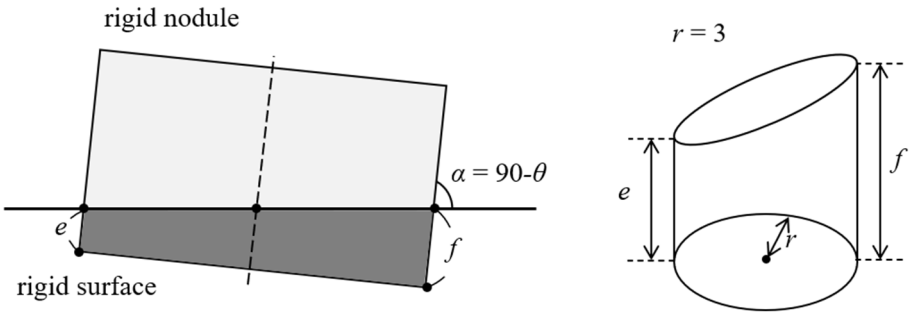

$$V = \pi r^2(e+f)/2$$

Figure 6. Interference volume of the rigid body nodules: (a) Definition of the interference volume, (b) interference volume at the beginning of the contact, (c) the interference volume at the end of the contact.

(a)

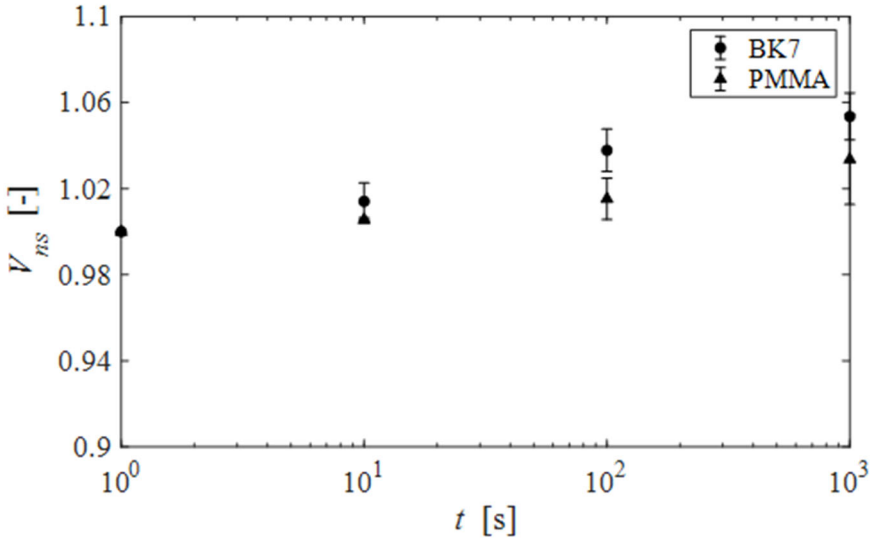

(b)

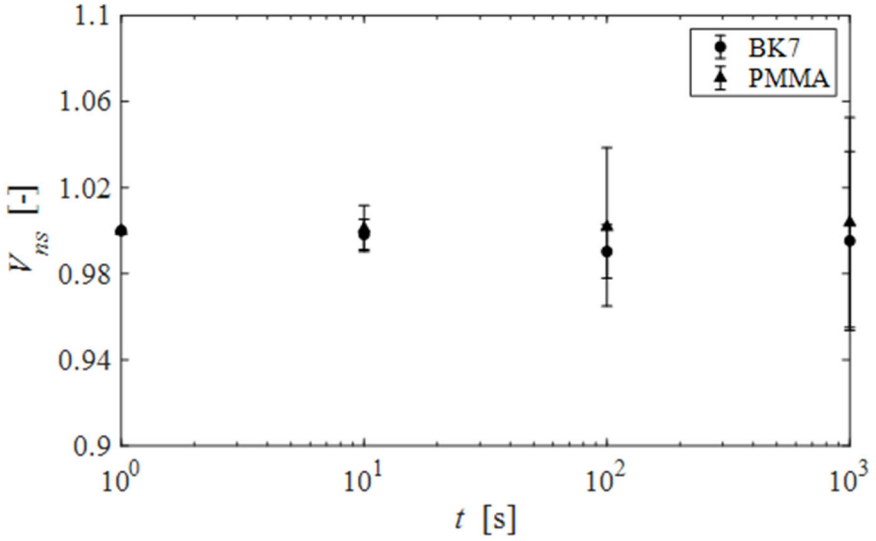

Figure 7. Temporal evolution of near-surface brush volume ratio V_{ns} in the stationary state. Here, V_{ns} of the relative value at t = 0 s. The brush was pushed 1 mm at 1 s, 10 s, 100 s, and 1000 s: (a) in the atmospheric conditions (b) in the liquid conditions.

(a)

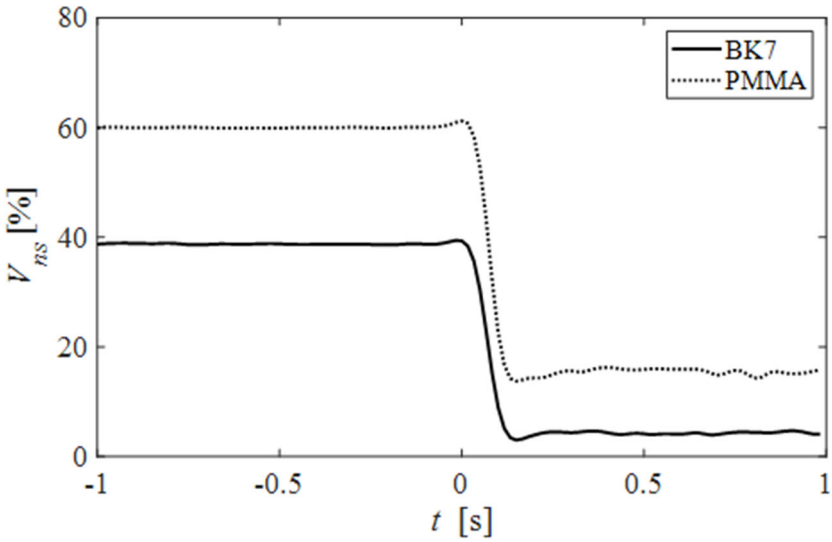

(b)

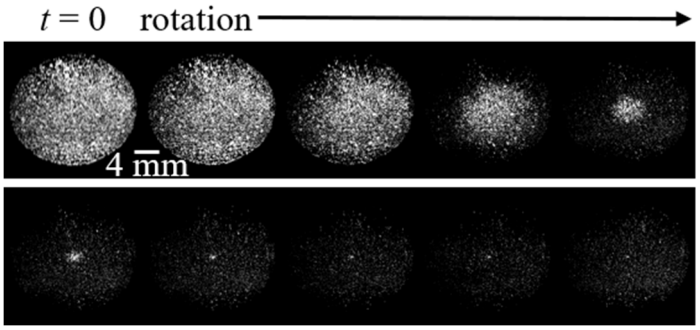

Figure 8. Brush near-surface existence at the beginning of rotation: (a) Near-surface cylindrical brush volume ratio V_{ns} (in liquid, visualization distance h = 300 nm, the brush starts rotating at t = 0 s), (b) Spatial and temporal change in brush near-surface existence on the BK7 prism. The white color indicates the part where the brush exists. See supplementary material[47] for a movie corresponding to Figure 8 (b).

Table 1. Observation conditions based on the brush type, prism, surface condition, and visualization distance for Fig. 9.

case	Surface material (Contact angle)	Brush type	Condition	Visualization distance *h*
a	BK7 (28°)	cylindrical	in liquid	50 nm
b				100 nm
c				200 nm
d				300 nm
e				400 nm
f			atmospheric	50 nm
g				100 nm

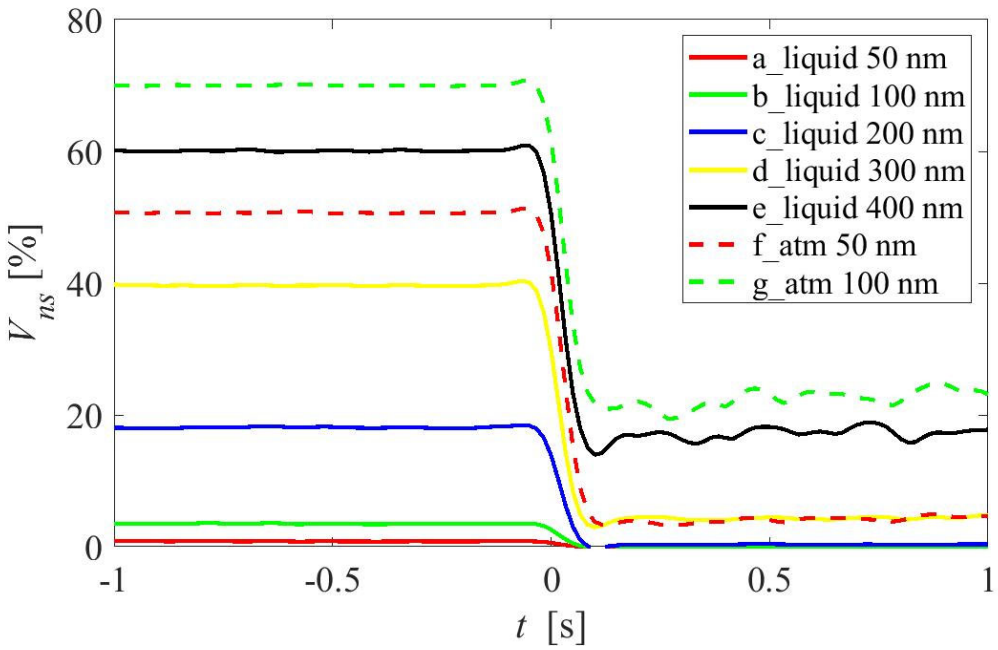

Figure 10. Near-surface brush volume ratio static and rotating conditions for different visualization distances on BK7 prism. The solid line and dashed line indicate liquid and atmospheric conditions, respectively. Cases a to g correspond to Table 1.

Table 2. Observation conditions based on the brush type, prism, surface condition, and visualization distance for Fig. 10.

case	Surface material (Contact angle)	Brush type	Condition	Visualization distance
a	BK7 (28°)	cylindrical	in liquid	300 nm
b	PMMA (61°)			
c	BK7 (28°)	roller		
d	PMMA (61°)			
e	BK7 (28°)	cylindrical	atmospheric	100 nm
f			in liquid	250 nm
g				545 nm

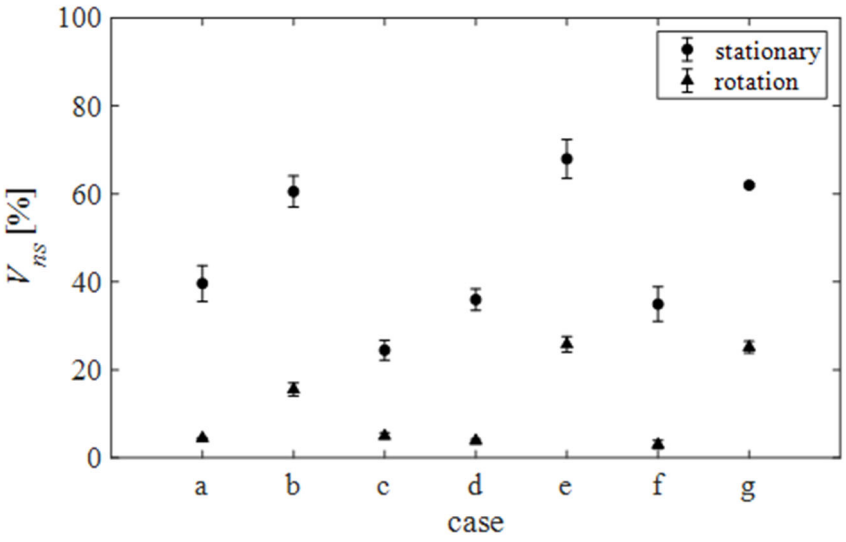

Figure 10. Near-surface brush volume ratio static and rotating conditions under various conditions. Cases a to g correspond to Table 2.

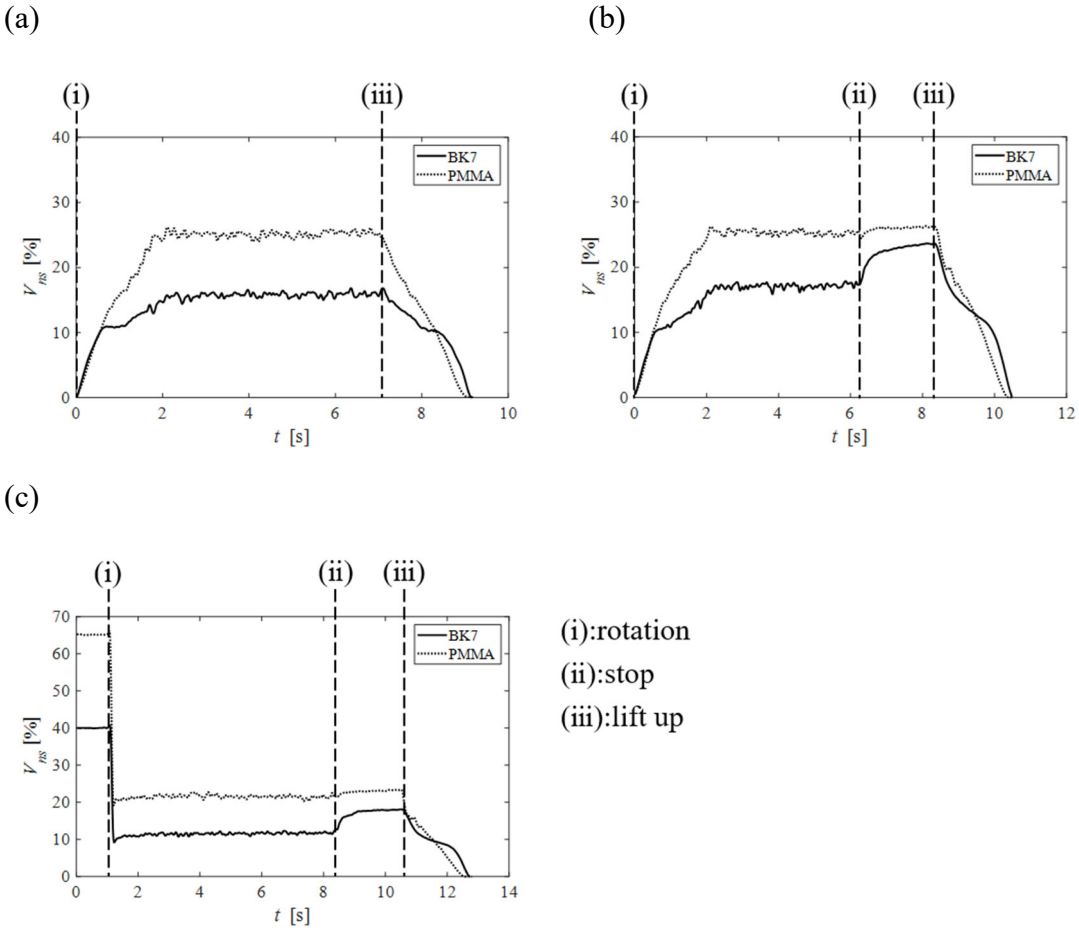

Figure 11. Near-surface cylindrical brush volume ratio during various movements: The time indicates (i) rotation start, (ii) rotation stop, and (iii) Brush lift-up. (a) brush contact under rotating and lift-up, (b) brush contact under rotating, rotation stops, and lift-up, (c) brush contact stationary, rotation starts, rotation stops, and lift-up. See supplementary material[48] for a movie corresponding to Figure 10 (c).

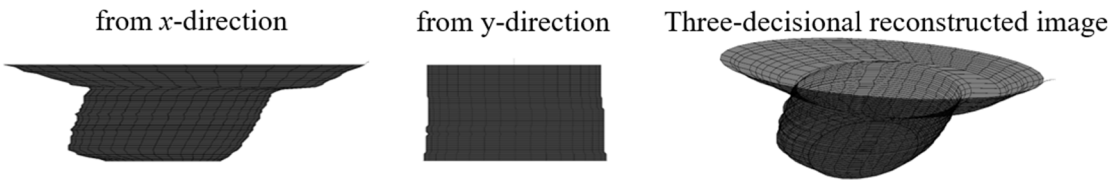

Figure 12. Stacked and reconstructed image of sliding roller brush’s nodules.

(a)

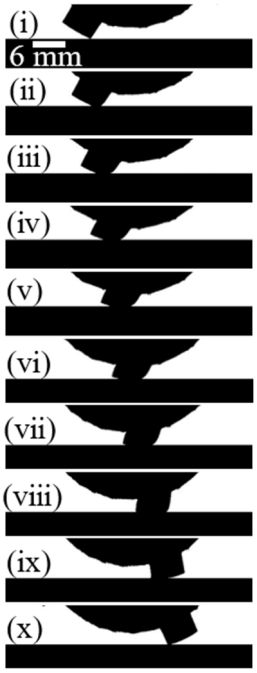

(b)

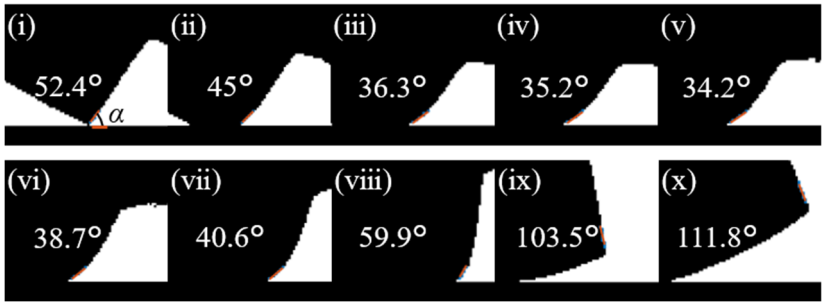

(c)

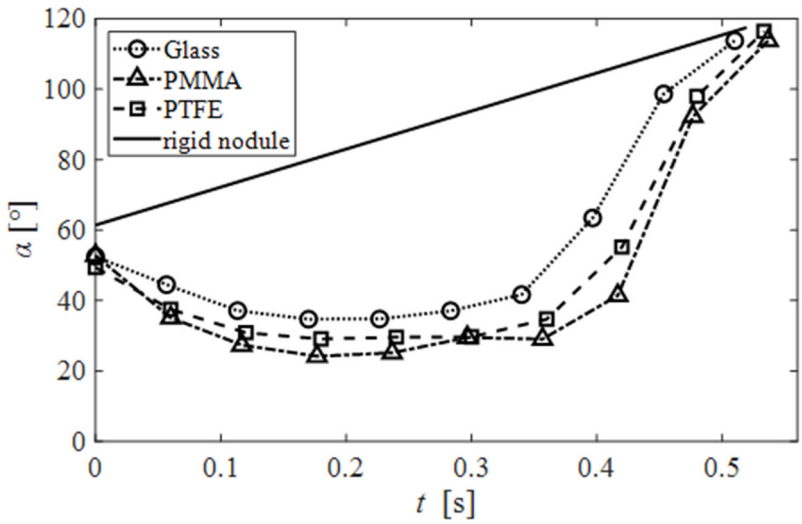

Figure 13. Nodule deformation during sliding: (a) continuous photographs of deformation taken from the *x*-direction (BK7, 20 rpm), (b) nodule front angle to the surface α (BK7, 20 rpm), (c) temporal change in the nodule front angle *α*.

(a)

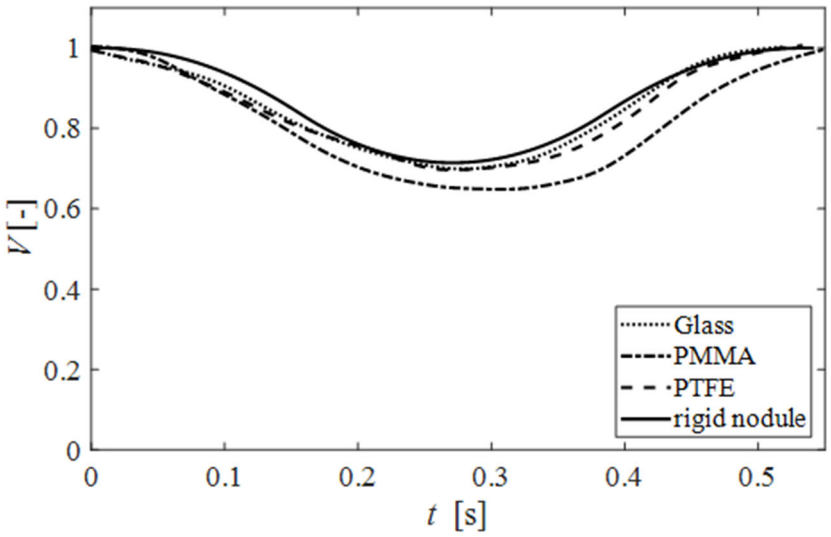

(b)

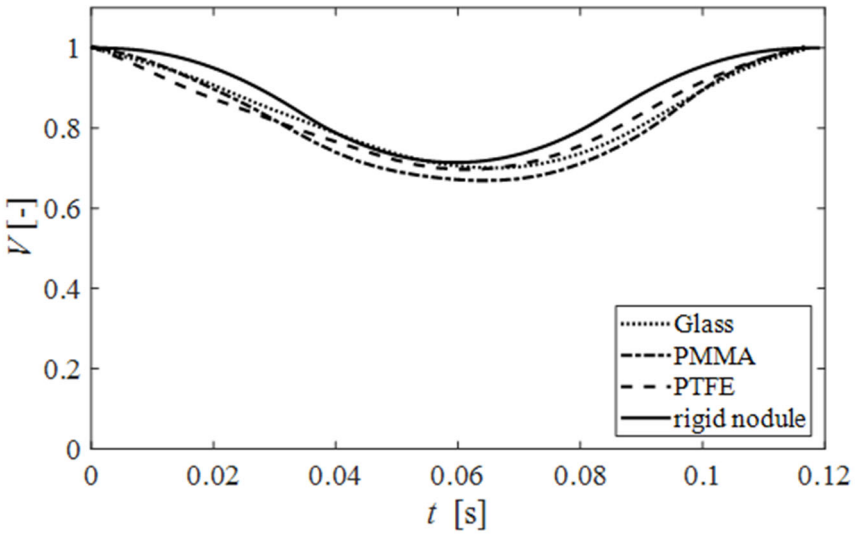

Figure 14. Nodule volume change during contacting and sliding compare to the rigid nodule's interference volume: (a) 20 rpm and (b) 80 rpm. The volume before contacting uses as a reference for normalization.